# Carbon Redistribution and Carbide Precipitation in a High-Strength Low-Carbon HSLA-115 Steel Studied on a Nanoscale by Atom Probe Tomography

CrossMark

DIVYA JAIN, DIETER ISHEIM, and DAVID N. SEIDMAN

HSLA-115 is a newly developed Cu-bearing high-strength low-carbon martensitic steel for use in Naval structural applications. This research provides, for the first time, a comprehensive compositional analysis of carbon redistribution and associated complex phase transformations in an isothermal aging study of HSLA-115 at 823 K (550 °C). Specifically, we characterize carbon segregation at lath boundaries, grain-refining niobium carbonitrides, cementite, and secondary hardening $M_2C$ carbides, in addition to copper precipitation, by 3D atom probe tomography (APT). Segregation of carbon (3 to 6 at. pct C) is observed at martensitic lath boundaries in the as-quenched and 0.12-hour aged microstructures. On further aging, carbon redistributes itself forming cementite and $M_2C$ carbides. Niobium carbonitride precipitates do not dissolve during the austenitizing treatment and are inherited in the as-quenched and aged microstructures; these are characterized along with cementite by synchrotron X-ray diffraction and APT. Sub-nanometer-sized $M_2C$ carbide precipitates are observed after the formation of Cu precipitates, co-located with the latter, indicating heterogeneous nucleation of $M_2C$. The temporal evolution of the composition and morphology of $M_2C$ carbides at 823 K (550 °C) is described using APT; their precipitation kinetics is intertwined with Cu precipitates, affecting the bulk mechanical properties of HSLA-115. Phase compositions determined by APT are compared with computed compositions at thermodynamic equilibrium using ThermoCalc.

## I. INTRODUCTION

LOW-CARBON (<0.06 wt pct) martensitic *high-strength low-alloy* (HSLA) steels replaced the higher carbon-containing *high-yield* (HY) steel grades as structural materials for Naval vessels during the 1980s.[1,2] The low carbon concentration of HSLA steels improves weldability, which reduces the preheating requirements and decreases considerably the processing cost.[3] To meet the strength requirements, Cu was added in HSLA-80 and HSLA-100 steels to utilize strengthening from Cu precipitates.[1,4,5] The numerals 80 and 100 denote the minimum obtainable tensile yield strength (YS) in ksi (1 ksi = 6.9 MPa). Since the approval of HSLA-100 for surface combatant ships in 1989, efforts were made by the US Navy to develop steels with similar compositions as HSLA-100 but with higher YS, while maintaining desirable impact toughness and weldability. These efforts led to the development of an HSLA-115 steel, the composition of which is slightly richer in Cu, Ni, and Mo than HSLA-100 (composition 2).[6] HSLA-115 was approved for plate production in 2009[6] and has been used in the flight deck of the CVN-78 aircraft carrier[7] and is the focus of this article.

Traditionally, commercial processing practices of HSLA-100 steels have employed an austenitizing, a water-quenching, and an aging treatment at temperatures exceeding 873 K (600 °C), which results in a tempered martensitic microstructure and over-aged Cu precipitates.[1,8] However, Wilson *et al.*[1] reported a rapid decrease in its YS for aging temperatures between 894 K and 950 K (621 °C and 677 °C), which limits its applications. In our recent article on HSLA-115,[9] we demonstrated that sub-nanometer-sized $M_2C$ carbides (M is Mo, Cr, Fe) can be co-precipitated with Cu precipitates in high number density ($\sim 10^{23}$ m$^{-3}$) during isothermal aging at 823 K (550 °C). This results in an extended YS plateau during aging, compared to alloys relying solely on Cu precipitation strengthening and can

DIVYA JAIN is with the Department of Materials Science and Engineering, Northwestern University, 2220 Campus Drive, Evanston, IL 60208. Contact e-mail: divyajain2016@u.northwestern.edu DIETER ISHEIM is with the Department of Materials Science and Engineering, Northwestern University, and also with the Northwestern University Center for Atom-Probe Tomography, 2220 Campus Drive, Evanston, IL 60208. DAVID N. SEIDMAN is with the Department of Materials Science and Engineering, Northwestern University, and also with the Northwestern University Center for Atom-Probe Tomography and the NanoAl LLC, Illinois Science + Technology Park, 8025 Lamon Ave, Suite number 446, Skokie, IL 60077.
Manuscript submitted January 30, 2017.
Article published online May 9, 2017

be used as a design principle to simultaneously optimize strength and impact toughness and develop higher strength steels.[9] Besides the two precipitating phases described above, grain-refining niobium carbonitride precipitates, Nb(C,N), and the embrittling cementite phase are other important microstructural constituents of HSLA-115 and similar HSLA-100 steels, which influence phase transformations and overall mechanical properties.[10] Microalloying additions of Nb (0.02 to 0.06 wt pct) to HSLA steels are performed to form Nb(C,N) precipitates, which pin austenite grain boundaries during hot rolling and austenitizing treatments and thus prevent excessive grain growth.[11,12] The dissolution of these precipitates has been shown to cause severe grain coarsening, as seen, for instance, in simulated weld heat-affected zones of HSLA-100 steel.[10,13] Thus, the stability of Nb(C,N) precipitates plays a key role in controlling grain size, which in turn affects hardenability, strength, and toughness properties. Cementite, alternatively, is associated with poor impact toughness properties of steels.[14] It forms due to the decomposition of retained austenite and low-carbon martensite and/or at the expense of the transient primary carbides, such as epsilon carbide, $Fe_{2.4}C$, and the eta carbide, $Fe_2C$.[15]

In this article, we provide systematic nanoscale analyses of carbon redistribution, segregation, and carbide precipitation for HSLA-115, isothermally aged at 823 K (550 °C), using 3D atom probe tomography (APT). 3D APT is a unique technique that provides three-dimensional spatial information of atoms as well as their chemical identities (including that of the lighter elements, such as carbon) with a sub-nanoscale spatial resolution.[16–18] We first describe the carbon redistribution that occurs during quenching after the austenitizing treatment, which in turn results in carbon segregation at martensitic lath boundaries. We then characterize niobium carbonitride and cementite precipitates in terms of their composition, morphology, and the partitioning behavior of various alloying elements between the α-Fe (b.c.c.) matrix and these precipitates; the evolution of these carbides is also investigated by synchrotron X-ray diffraction experiments, performed at the Advanced Photon Source. Lastly, we describe, in detail, the temporal evolution of the composition and morphology of $M_2C$ carbides at 823 K (550 °C). Their evolution in terms of mean radii, number densities, and volume fractions has been described recently in correlation with the mechanical properties in our companion paper.[9] APT-measured chemical compositions of the carbide precipitates—niobium carbonitride, cementite, and $M_2C$ carbide (at long aging times)—are also compared with the respective computed compositions at thermodynamic equilibrium using ThermoCalc.

In recent years, quantitative information from APT experiments combined with the theory-driven computational design-based approach has been used to design a blast-resistant BA-160 steel, which is a low-carbon martensitic steel, precipitation-strengthened by Cu precipitates and $M_2C$ carbides.[19–21] Precipitate size distributions obtained in 3D from APT can be used to develop models, predicting the YS of precipitation-hardened alloys.[22] APT with its sub-nanoscale spatial resolution allows one to determine the concentrations of alloying elements at the heterophase interfaces and at the grain boundaries, which helps in understanding the kinetics of complex phase transformations, such as grain boundary precipitation[23] and growth mode of cementite during tempering of steels.[24] Using APT, one can detect precipitates at early aging times and hence determine the temporal evolution of their compositions, which can provide deep insights into their nucleation kinetics[25] and has also been suggested to be useful in estimating the remnant lifetime of steel components in power plant steels.[26]

## II. EXPERIMENTAL METHODS

The overall chemical composition of HSLA-115 steel, as measured using optical emission spectroscopy, is displayed in Table I. HSLA-115 steel samples were subjected to two consecutive austenitizing treatments of 35 minutes each at 1185 K (912 °C), and each austenitizing treatment was followed by water quenching to room temperature. Multiple austenitizing treatments with shorter holding times, as compared to single austenitization of the same total duration, reduce the formation of large isolated austenite grains.[1] The as-quenched samples were then isothermally aged at 823 K (550 °C) for aging times ranging from 0.12 to 256 hours and were then water quenched to room temperature. High-intensity synchrotron X-ray diffraction (XRD) scans were performed on the polished samples having a final polish of 0.06 μm colloidal silica at the 5-IDB beamline at the Advanced Photon Source (Argonne National Laboratory, Argonne, IL, USA). Scans were performed from 2θ ranging from 9.995 to 33.500 deg using a step size of 0.015 deg, a count time of 3 s per step, and a wavelength of 0.71 Å. At each step, the sample was rocked through 0.75 deg in θ to reduce preferential orientation effects. Nanotips for APT experiments were prepared by first cutting blanks with the dimensions of approximately $0.3 \times 0.3 \times 10$ $mm^3$. These blanks were then electropolished at room temperature using a two-step electropolishing procedure, the details of which are provided in our companion paper.[9] APT experiments were performed with a Cameca local electrode atom probe (LEAP) 4000X-Si tomograph, using a pulsed ultraviolet (wavelength = 355 nm) picosecond laser, with an energy of 30 pJ per pulse, a pulse repetition rate of 500 kHz, and an average evaporation rate (number of ions per pulse) of 2 pct. The samples were analyzed at a specimen base temperature of 60 K (−213 °C) in ultrahigh vacuum ($<10^{-8}$ Pa) and the data obtained were analyzed using the program IVAS 3.6 (Cameca, Madison, WI). The chemical compositions of the different microstructural features, identified by APT, are obtained using the proximity histogram (proxigram) concentration profile method[27] and the errors reported are ±2σ, where σ is obtained from counting statistics[28] and is given by

$$\sigma = \sqrt{\frac{c_i(1-c_i)}{N}}, \qquad [1]$$

**Table I. Chemical Composition of HSLA-115, as Measured by Optical Emission Spectroscopy**

| Elements | Fe | Cu | Ni | Mn | Si | Al | Mo | Cr | Nb | C | V | N |
|---|---|---|---|---|---|---|---|---|---|---|---|---|
| Wt Pct | bal. | 1.29 | 3.37 | 0.97 | 0.22 | 0.02 | 0.56 | 0.64 | 0.02 | 0.05 | <0.01 | 0.016 |
| At. Pct | bal. | 1.13 | 3.21 | 0.99 | 0.44 | 0.04 | 0.33 | 0.69 | 0.012 | 0.23 | <0.01 | 0.064 |

**Table II. Tensile Test Results at Room Temperature for HSLA-115 in the As-quenched Condition and After Aging at 823 K (550 °C) for 0.25, 1, 3, and 16 h, data from Jain et al.[9]**

| Aging Time (h) | YS (MPa) | UTS (MPa) | Elongation to Failure (Pct) |
|---|---|---|---|
| As-quenched | 856.3 ± 20.6 | 1119.2 ± 6.9 | 18.5 ± 1.0 |
| 0.25 | 986.8 ± 11.8 | 1034.5 ± 12.2 | 21.4 ± 0.6 |
| 1 | 967.6 ± 14.3 | 1004.2 ± 7.0 | 22.4 ± 0.7 |
| 3 | 972.1 ± 7.5 | 997.2 ± 9.8 | 24.8 ± 1.0 |
| 16 | 911.4 ± 3.4 | 939.5 ± 6.6 | 22.2 ± 0.6 |

where $c_i$ is the measured concentration of element $i$ and $N$ is the total number of atoms in the sampled volume. It is noted that the average composition of the different microstructural features is determined after taking the weighted average of their core concentrations (based on the total number of atoms). Since the analyzed volume decreases significantly (smaller number of total atoms, $N$) toward the core of the microstructural features, the weighted average is a more accurate representation of their composition.

The APT mass spectra of the carbide precipitates—Nb(C,N), cementite, and $M_2C$ carbides—are also presented in this paper, since it is important to explain in detail how the compositions of these phases were obtained, which is not trivial due to critical isobaric peak overlaps and various complex molecular ion peaks in these mass spectra. Thermodynamic calculations are performed using ThermoCalc, version S, and the thermodynamic data are obtained from the TCFE6 steel database (SGTE).

## III. RESULTS AND DISCUSSION

### A. Mechanical Properties

Tensile yield strength (YS), ultimate tensile strength (UTS), and elongation to failure for HSLA-115 (at room temperature) in the as-quenched condition and for samples aged at 823 K (550 °C) for different aging times are listed in Table II. The YS values are also plotted with Charpy impact energy [measured at 255 K (−17.8 °C)] for these samples in Figure 1. These results reveal an increase of 67 pct in impact toughness after 3-hour aging from its value obtained in the 0.25-hour aged condition, with a negligible decrease of 1.5 pct in YS. More detailed discussion on these mechanical properties is provided in our companion paper,[9] where we correlated the co-precipitation of $M_2C$ carbides with Cu precipitates in HSLA-115 to this extended YS plateau attained during aging at 823 K (550 °C).
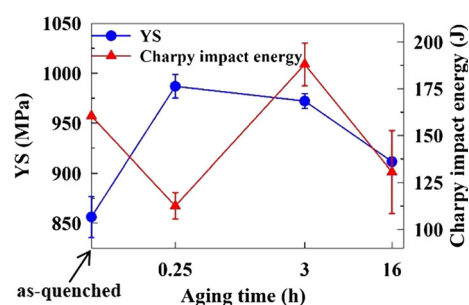


Fig. 1—Yield strength (YS) at room temperature and Charpy impact energy at 255 K (−17.8 °C) for HSLA-115 in the as-quenched condition and after aging at 823 K (550 °C) for 0.25, 3, and 16 h, data from Jain et al.[9]

### B. Synchrotron X-ray Diffraction (XRD)

Figure 2 shows the XRD scans for HSLA-115 in the as-quenched condition, and for samples aged at 823 K (550 °C) for 0.25, 3, and 16 hours. We observe reflections corresponding to niobium carbide (NbC) in the as-quenched sample as well as in all the aged samples, Figure 2(a). Cementite ($\theta_{cem}$) peaks are not observed in the as-quenched sample but are present in all the aged samples, Figure 2(a), confirming the formation of cementite during aging at 823 K (550 °C). It is noted that the low overall carbon concentration of HSLA-115 (0.23 at. pct or 0.05 wt pct) limits the volume fraction of these carbides to less than 1 pct. Additional difficulty arises in characterizing cementite due to the overlap of its largest intensity reflection with that of $(110)_\alpha$ reflection.[27] Volume fraction of austenite in the as-quenched sample, as calculated using the direct comparison method,[29] is less than 1 pct. Low volume fraction of retained austenite is anticipated in the as-quenched microstructure of such low-carbon low-alloy steels and is in agreement with the findings for similar HSLA-100 steels.[30] Additionally, this retained austenite is unstable on aging, as is evident from the decrease in the intensity of the $(200)_\gamma$ reflection in the XRD scans of the aged samples, Figure 2(b).
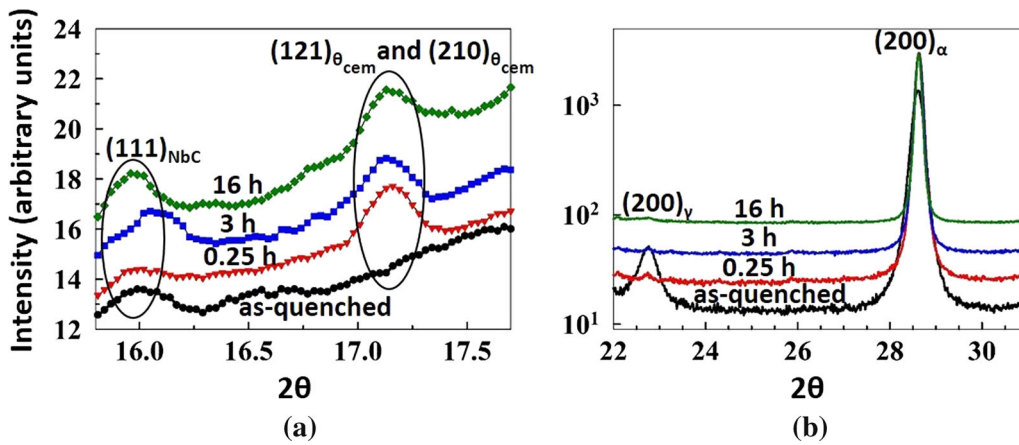
Fig. 2—Synchrotron X-ray diffraction scans of the as-quenched HSLA-115 sample and those aged at 823 K (550 °C) for 0.25, 3, and 16 h. The subscripts $\theta_{cem}$ and NbC on the reflection indices in (a) refer to niobium carbide and cementite, respectively, while the subscripts $\gamma$ and $\alpha$ in (b) refer to austenite and ferrite, respectively.
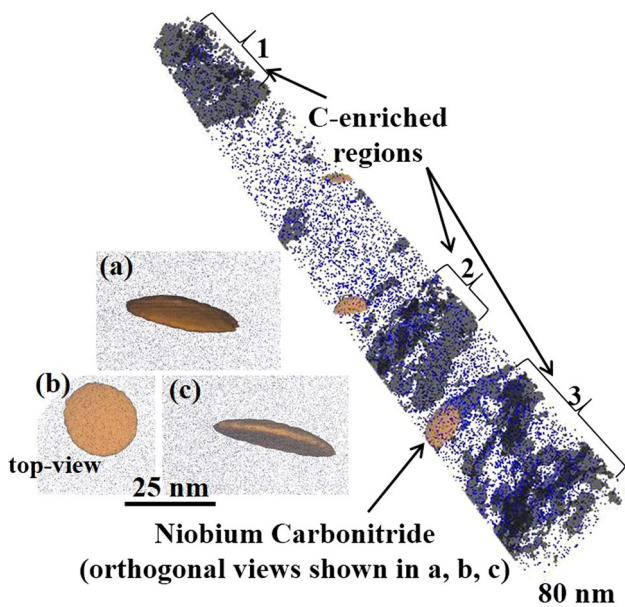


Fig. 3—3D APT reconstruction of the as-quenched HSLA-115 sample. C-enriched regions are delineated by 1 at. pct C isoconcentration surfaces (black). Niobium carbonitride precipitates are delineated by 15 at. pct (Nb + C) isoconcentration surfaces (brown). Only a fraction of the Fe atoms are displayed (blue dots) and the other alloying element atoms are omitted for the sake of clarity (Color figure online).
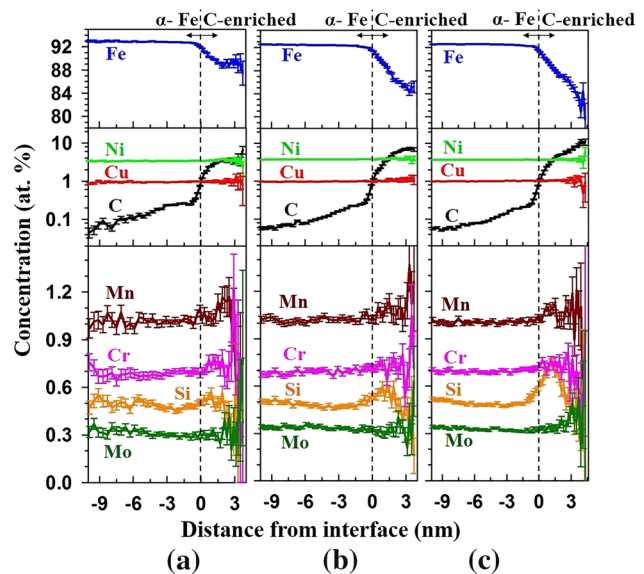


Fig. 4—Proximity histogram concentration profiles (at. pct) of Fe, C, Ni, Cu, Mn, Cr, Si, and Mo for C-enriched regions 1, 2, and 3 in Fig. 3 and their vicinity are displayed in (a), (b), and (c), respectively. These C-enriched regions are delineated by 1 at. pct C isoconcentration surfaces in Fig. 3, which is the 3D APT reconstruction of the as-quenched HSLA-115 sample. Ordinate axis of the plots displaying C, Ni, and Cu concentration profiles is drawn on a log scale for clear visualization of the C concentrations in α-Fe matrix in the vicinity of C-enriched regions.

## C. Atom Probe Tomography

### 1. Carbon segregation at martensitic lath boundaries

We observed the enrichment of carbon at several regions in the 3D APT reconstruction of the as-quenched sample, Figure 3. These C-enriched regions are marked as 1, 2, and 3 in Figure 3 and are delineated by 1 at. pct C isoconcentration surfaces. Proximity histogram (proxigram) concentration profiles with respect to distance from these isoconcentration surfaces are displayed in Figures 4(a), (b), and (c) for regions 1, 2, and 3, respectively.

Carbon concentrations in the core of the C-enriched regions (~2-nm region at the far right-hand side of the

proximity histograms in Figure 4) are 3.6 ± 0.1, 6.2 ± 0.1, and 6.4 ± 0.1 at. pct for regions 1, 2, and 3, respectively, while the average carbon concentration of the α-Fe matrix in proximity of these regions, as obtained from the 2.5-nm region at the far left-hand side of the proximity histograms in Figure 4, is 0.06 ± 0.01 at. pct. It is noted that the methodology described by Geuser et al.[31] that uses the distribution of isolated atoms in atom probe reconstructions provides an alternative method to determine the matrix concentrations of alloying elements. However, detailed analysis using this method is beyond the scope of this work since

proximity histogram concentration profiles provide the C concentrations in the C-enriched regions as well as in the α-Fe matrix, as a function of distance from the interface between them.

Concentration profiles in Figure 4 also reveal that the enrichment of carbon results mainly in the depletion of Fe in these regions, while the alloying elements—Ni, Cu, Mn, Cr, and Mo—exhibit negligible partitioning between the α-Fe matrix and C-enriched regions. Silicon, however, behaves differently as its concentration is enhanced near the interface with respect to its α-Fe matrix concentration (most prominent in Figure 4(c)), but decreases toward the inner core of the C-enriched regions at the far right-hand side of the concentration profile. This is suggestive of Si being rejected from these C-enriched regions.

Several other studies have also reported similar C-enriched regions with varying carbon concentrations from 2 to 10 at. pct, and have interpreted their results as carbon segregation at martensitic lath boundaries or as thin austenitic films at these boundaries.[32–36] Carbon segregation in the as-quenched sample suggests that carbon diffusion occurs from the freshly formed martensite during quenching. This process is facilitated due to the extremely low solubility of carbon in lath martensite,[37] coupled with a high martensite start temperature ($M_s$) of HSLA-115. The $M_s$ temperature of HSLA-115, as calculated from Andrew's empirical formula, is 705 K (432 °C),[38] which is in good agreement with the measurements of the $M_s$ temperature of ~693 K (420 °C) for similar HSLA-100 steels from dilatometry experiments.[1,10] While APT provides direct evidence of carbon segregation, the same conclusion has been made based on electrical resistivity measurements by Speich,[39] who suggested that most of the carbon segregates to dislocations and lath boundaries in low-carbon as-quenched lath martensites (C < 0.2 wt pct). In the present study, we also measure much lower carbon concentration of 0.08 at. pct in the α-Fe matrix (excluding the C-enriched regions), as compared to 0.21 at. pct C measured for the entire analyzed volume of the as-quenched APT sample, which is close to the alloy's overall carbon concentration, 0.23 at. pct, Table III.

A similar C-enriched region is also observed in the HSLA-115 sample aged at 823 K (550 °C) for 0.12 hours. This is evident from the distribution of carbon atoms shown in the two orthogonal views of the 3D APT reconstruction of this sample, Figure 5(a). Copper precipitates are also observed at this aging time and are delineated by 7 at. pct Cu isoconcentration surfaces. Proximity histogram concentration profiles with respect to distance from 1 at. pct C isoconcentration surfaces are displayed in Figure 5(b). We obtain a carbon concentration of 2.7 ± 0.1 at. pct in the core of the C-enriched region (~1-nm region at the far right-hand side of the proxigram), which is comparatively less than the carbon concentrations measured in similar regions in the as-quenched sample. Additionally, we observe the enrichment of Mn, Cr, and Mo in the C-enriched region in this 0.12-hour aged sample, Figure 5(b), which is in contrast to the homogeneous distributions of these elements observed across the α-Fe
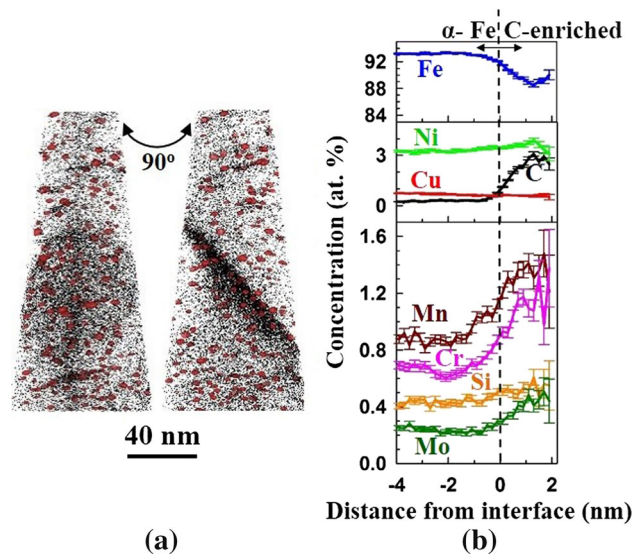


Fig. 5—(a) 3D APT reconstruction (two orthogonal views) of the HSLA-115 sample aged at 823 K (550 °C) for 0.12 h. Carbon atoms are displayed as black dots, Cu precipitates are delineated by 7 at. pct Cu isoconcentration surfaces (red), and the other alloying element atoms are omitted for the sake of clarity; (b) proximity histogram concentration profiles (at. pct) of Fe, C, Ni, Cu, Mn, Cr, Si, and Mo for C-enriched region in (a) and its vicinity (excluding the Cu precipitates, which were removed from the dataset before the proxigram analysis using the IVAS program) (Color figure online).

matrix and the C-enriched regions in the as-quenched sample, Figure 4.

### 2. Niobium carbonitride precipitates

Three niobium carbonitride precipitates are observed in the 3D APT reconstruction of the as-quenched sample and are delineated by 15 at. pct (Nb + C) isoconcentration surfaces (brown), Figure 3. Two of the niobium carbonitride precipitates are dissected in the 3D reconstruction, while the third one lies completely inside it and is indicated by an arrow, Figure 3. Three orthogonal views of this precipitate are also displayed in this figure; the precipitate appears to have a thin platelet-like morphology, which has been reported earlier in other APT[40–42] and TEM[43] studies of Nb-containing steels. The APT mass spectrum of this precipitate is displayed in Figure 6(a). Carbon peaks are obtained corresponding to $C^{2+}$, $C^+$, $C_3^{2+}$, and $C_2^+$ ions, while niobium is detected as $Nb^{4+}$, $Nb^{3+}$, and $Nb^{2+}$ and as molecular ions—$(NbN)^{3+}$ and $(NbN)^{2+}$ along with nitrogen. The peak at 14 amu contributes 3.7 at. pct of the total number of atoms associated with this precipitate and is taken as $^{14}N^+$, although there may be some contribution from $^{28}Si^{2+}$. We note that a number of molecular ion peaks, identified herein, may easily be overlooked and/or the ionic peaks may be wrongly assigned in the bulk mass spectrum of the sample due to the extremely low overall Nb concentration (0.012 at. pct) in this alloy. For instance, the peak at 31 amu can be incorrectly assumed to be $^{62}Ni^{2+}$, if we analyze the precipitate using the mass spectrum of the bulk sample. For an accurate analysis, Nb(C,N) precipitates should first be isolated from the rest of the matrix and then the
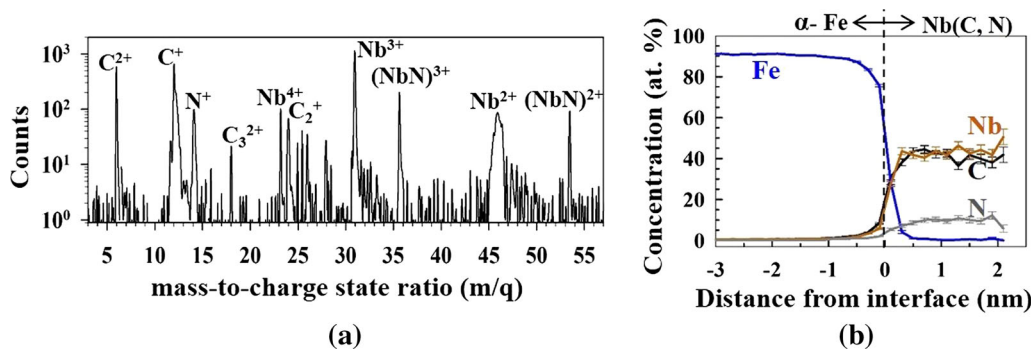
Fig. 6—(a) Atom probe tomographic mass spectrum of the niobium carbonitride precipitate, observed in the as-quenched HSLA-115 sample, which is indicated by an arrow in Fig. 3. Mass peaks associated with Nb, C, and N are labeled in the mass spectrum, while those of other minor elements in the precipitate, such as Fe, Mo, Cr, and V, are not labeled for the sake of clarity; (b) proximity histogram concentration profiles (at. pct) of Fe, Nb, C, and N for the niobium carbonitride precipitate and its vicinity. A fiducial marker is placed vertically at the origin (0) of the proxigram, which is chosen as the inflection point of the Fe concentration profile.

**Table III. Chemical Composition (At. Pct) of the Niobium Carbonitride Precipitate Observed in the As-quenched HSLA-115 Sample, as Obtained from APT Measurements**

| Element | Nb | C | N | Fe | Mo | Cr | V |
|---|---|---|---|---|---|---|---|
| APT-Measured Composition | $43.2 \pm 1.4$ | $41.6 \pm 1.4$ | $9.8 \pm 0.8$ | $0.5 \pm 0.2$ | $2.7 \pm 0.4$ | $1.1 \pm 0.3$ | $0.5 \pm 0.20$ |
| Computed Composition, ThermoCalc | 40.7 | 15.4 | 34.5 | 0.02 | 0.05 | 2.1 | 7.2 |

Equilibrium composition of niobium carbonitride from thermodynamic computations at 1185 K (912 °C) is also displayed.

analysis of the spatially segmented mass spectrum should be performed separately to ensure correct identification of all mass peaks.

Thermodynamic equilibrium calculations for HSLA-115 predict that Nb(C,N) precipitates dissolve above 1408 K (1135 °C) but are stable at the austenitizing temperature of 1185 K (912 °C) and are thus effective in inhibiting grain growth during the austenitizing treatment. Thus, the precipitates obtained in the as-quenched sample are likely inherited from the austenitizing treatment. Proximity histogram showing the concentration profiles of Fe, Nb, C, and N across the hetero-interface between α-Fe matrix and the Nb(C,N) precipitate is displayed in Figure 6(b). Table III lists the composition of the Nb(C,N) precipitate obtained from this proximity histogram along with its computed composition at thermodynamic equilibrium at 1185 K (912 °C). From APT analysis, we obtain a combined contribution of 51.4 at. pct from C and N, while the metal composition is primarily Nb with some Mo, Cr, V, and Fe. While the Nb concentration in the precipitate, as measured by APT (43.2 at. pct), is in reasonably good agreement with the predicted concentration from thermodynamic equilibrium calculations (40.7 at. pct), the concentrations of the interstitial solute elements, C and N, differ significantly between the two methods.

Thermodynamic equilibrium calculations at the austenitizing temperature of 1185 K (912 °C) reveal that the C concentration in Nb(C,N) precipitates increases at the expense of N if the available

concentration of N decreases from its overall bulk concentration of 0.016 wt pct; this trend holds even for lower bulk C concentrations than the 0.05 wt pct in this steel. For instance, for bulk C concentration of 0.04 wt pct and bulk N concentrations of 0.012, 0.008, and 0.004 wt pct, equilibrium calculations predict 26.9, 20.1, and 15.7 at. pct N and 22.9, 29.7, and 33.9 at. pct C, respectively, in Nb(C,N) precipitates. Thus, we infer that less than 0.016 wt pct N is available during the austenitizing treatment as it may have combined with pre-existing Nb(C,N) precipitates formed during prior processing treatment steps, and this likely is the reason that we obtain higher C concentration than N in the Nb(C, N) precipitates analyzed by APT.

Additionally, the predicted equilibrium composition overestimates V and to a smaller extent Cr in the precipitate and underestimates the Mo and Fe concentrations. It also predicts negligible solubility of Si in niobium carbonitride, which makes it reasonable to assign the peak at 14 amu in the APT mass spectrum to $^{14}N^+$.

In the present study, we also observe a Nb(C,N) precipitate in the APT reconstruction of the 16-hour aged sample. XRD results described earlier revealed the presence of niobium carbide in the as-quenched sample and in the samples aged at 823 K (550 °C) for 0.25, 3, and 16 hours, Figure 2(a). These precipitates are, however, only observed in the 3D APT reconstructions of the as-quenched and the 16-hour aged samples due to their low number densities.
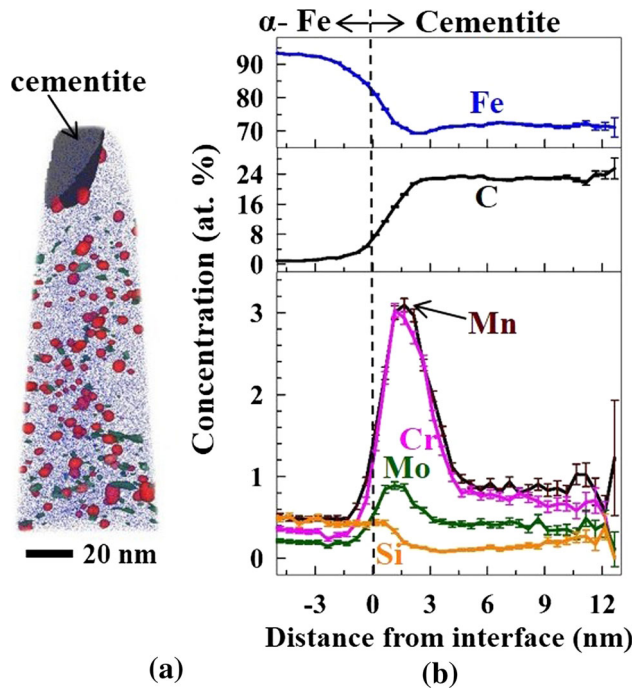
Fig. 7—(a) 3D APT reconstruction of the HSLA-115 sample aged at 823 K (550 °C) for 0.25 h. The cementite precipitate is delineated by a 5 at. pct C isoconcentration surface (black). Copper precipitates and $M_2C$ carbides are delineated by 10 at. pct Cu isoconcentration surfaces (red) and 5 at. pct (C + Cr + Mo) isoconcentration surfaces (dark green), respectively. Only a fraction of the Fe atoms are shown (blue dots) and the other alloying element atoms are omitted for the sake of clarity; (b) proximity histogram concentration profiles (at. pct) of Fe, C, Mn, Cr, Mo, and Si for the cementite precipitate and its vicinity. A fiducial marker is placed vertically at the origin (0) of the proxigram, which is chosen as the inflection point of the Fe concentration profile (Color figure online).

### 3. Cementite precipitate

A cementite ($\theta_{cem}$) precipitate is observed in the 3D APT reconstruction of the 0.25-hour aged sample at 823 K (550 °C) and is delineated by a 5 at. pct C isoconcentration surface, Figure 7(a). Also, displayed in this APT reconstruction are the Cu precipitates (red) and $M_2C$ carbides (dark green). C-enriched regions observed in the as-quenched and 0.12-hour aged samples, Figures 3 and 5(a), respectively, and/or the decomposition of the retained austenite and lath martensite in the as-quenched microstructure are the likely sources of carbon for cementite formation during aging at 823 K (550 °C). The cementite precipitates' coarser morphology relative to the $M_2C$ carbides is evident in Figure 7(a) and is usually associated with poor impact toughness.[14] In our companion paper,[9] we discussed the possible role of the cementite phase in the poor impact toughness that results after 0.25-hour aging as compared to the as-quenched sample: Figure 1 in the present article. Here, we focus on the concentrations and the partitioning behavior of alloying elements across the $\alpha$-Fe/$\theta_{cem}$ hetero-interface, obtained using the proximity histogram displayed in Figure 7(b).

Analysis of the mass spectrum of the cementite precipitate revealed carbon peaks at 6, 12, 18, 24, 36, and 48 amu that correspond to $C^{2+}$, $C^+$, $C_3^{2+}$, $C_2^+$ or
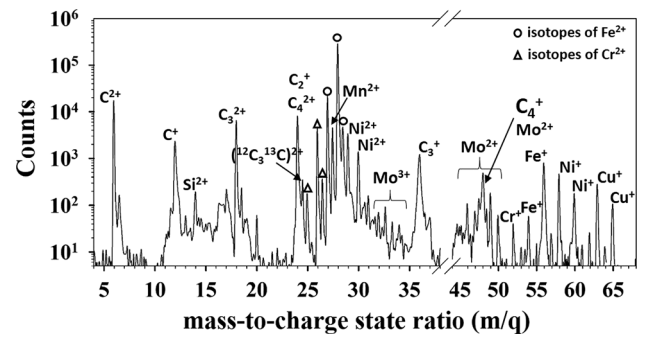


Fig. 8—Atom probe tomographic mass spectrum of the cementite precipitate observed in the HSLA-115 sample aged at 823 K (550 °C) for 0.25 h.

$C_4^{2+}$, $C_3^+$, and $C_4^+$ ions, respectively, Figure 8. These include overlaps of $C_2^+$ and $C_4^{2+}$ at 24 amu and of $C_4^+$ and $Mo^{2+}$ at 48 amu. Contribution of $C_4^{2+}$ to the counts at 24 amu is inferred by the mass peak at 24.5 amu, which corresponds to $(^{12}C_3^{13}C)^{2+}$. We also observe that counts at 48 amu exceed the counts at 49 amu, which contradicts the relative natural isotopic abundances for $Mo^{2+}$. This indicates additional contributions from the other ions at 48 amu, which is most likely $C_4^+$. The individual contributions of the overlapping ions at 24 and 48 amu were determined following the methodology of relative isotopic abundances, described by Sha et al.[44] for a binary Fe-C alloy.

In the proximity histogram, Figure 7(b), we obtain localized concentration peaks of Mn, Cr, and Mo having a width of a few nanometers near the $\theta_{cem}$/$\alpha$-Fe interface, with their peak concentrations of $3.0 \pm 0.2$, $3.0 \pm 0.2$, and $0.9 \pm 0.1$ at. pct, respectively. The diffusion distances of Mn, Cr, Mo, and Si for 0.25 hours at 823 K (550 °C), estimated by one-dimensional root-mean-squared distance, $\sqrt{2Dt}$ are 20, 14, 5, and 38 nm, respectively, and are three-to-four orders of magnitude smaller than that of carbon. Diffusion constants ($D$) of these elements in $\alpha$-Fe at 823 K (550 °C) are listed in Table IV along with the corresponding references.[45–49] These diffusion distances, particularly of Mn, Cr, and Mo, reveal the sluggish diffusion kinetics of these elements, which results in their localized concentration peaks observed near the $\theta_{cem}$/$\alpha$-Fe interface. We note, however, that even the peak concentrations of Mn and Cr (~3 at. pct each) obtained from the APT analysis are significantly less than their respective concentrations of 9.1 and 23.9 at. pct in cementite, computed by considering thermodynamic metastable equilibrium between ferrite and cementite at 823 K (550 °C), Table V. However, these locally enriched concentrations do indicate that the growth of cementite precipitate is in an intermediate stage between paraequilibrium (partitioning of only interstitial species (carbon) occurs as per equilibrium thermodynamics) and orthoequilibrium (partitioning of all elements including the substitutional ones occurs).[50] A similar growth mode of cementite was also reported in an atom probe study of an Fe-1.0C-0.30Si-0.2Mn-1.4Cr (wt pct) steel, aged isothermally at 773 K (500 °C).[51]

In the core of the cementite precipitate (6-nm region at the far right-hand side of the proxigram in Figure 7(b)), we observe nearly homogeneous distribution of all elements and the average composition of this region is displayed in Table V. We note that the carbon concentration in the core of the cementite precipitate is $22.7 \pm 0.2$ at. pct, as opposed to the stoichiometric value of 25.0 at. pct. Similar and much lower levels of carbon in cementite have been reported in other atom probe studies.[52–54] Carbon concentrations can be underestimated during APT analysis due to the losses that can occur due to multiple detection events, and in particular if field evaporation leads to the formation of molecular species and potentially their dissociation.[55,56] Partitioning ratios of elements, defined as the ratio of their concentration in the core of the cementite precipitate to their concentrations in $\alpha$-Fe matrix,[57] are also listed in Table V. Partitioning ratios for each of Mn, Cr, and Mo are greater than 1.5, indicating their enrichment in the cementite precipitate. Alternatively, Si partitions away from the cementite and has a partitioning ratio of 0.3. It is noted that its minimum concentration in the cementite precipitate is $0.08 \pm 0.02$ at. pct (at ~3.6 nm from the origin of the abscissa), which gradually increases to 0.16 at. pct in the core of the precipitate. Silicon is known to suppress the formation of cementite during tempering in steels.[53,58,59] It is believed that the rejection of Si from cementite results in the increase in the activity of carbon in Si-rich regions (in proximity of cementite), which reduces the carbon flux toward cementite and restricts its further growth.[58,59] In general, the partitioning behavior of alloying elements, observed herein, in terms of their enrichment/depletion is consistent with other studies, which have also reported the enrichment of Mn,[24,41,52,54,60,61] Cr,[24,54,61] and Mo[24] and depletion of Si[24,41,52–54,60,61] in cementite with respect to their respective concentrations in the $\alpha$-Fe matrix.

### 4. *Temporal evolution of Cu precipitates and $M_2C$ carbides at 823 K (550 °C)*

The precipitation kinetics of Cu precipitates and $M_2C$ carbides in HSLA-115 aged at 823 K (550 °C) are closely interlinked with one another. Nucleation of Cu precipitates occurs first, Figure 9(a), and is followed by the precipitation of $M_2C$ carbides with longer aging times, most of which are co-located with Cu precipitates, Figures 9(b) through (e). This indicates that Cu precipitates act as heterogeneous nucleation sites for $M_2C$ carbides; similar observations for Cu precipitates and $M_2C$ carbides have been reported for a BA-160 steel[21] and an ultrahigh-strength carburized steel.[62] We also observe a second burst of nucleation of both Cu precipitates and $M_2C$ carbides between 1 and 3 hours of aging at 823 K (550 °C); see Tables VI and VII, respectively, for the temporal evolution of their mean radii, number densities, and volume fractions. The complex kinetics of these precipitates, as observed herein, is likely affected by the interactions of these precipitates with each other and with dislocations and lath boundaries in the microstructure. This was discussed in correlation with the mechanical properties of HSLA-115 in our companion paper.[9] Herein, we describe the temporal evolution of the morphologies and compositions of Cu precipitates and $M_2C$ carbides at 823 K (550 °C). As the main focus of this article is carbon redistribution and carbide precipitates, the temporal evolution of Cu precipitates is only briefly described.

It is known that Cu nucleates as coherent (b.c.c.) spheroidal precipitates in $\alpha$-Fe.[63–65] As Cu precipitates grow and coarsen upon aging, they undergo shear transformations to 9R and 3R structures and finally transform to the equilibrium f.c.c. structure.[66,67] As their size increases, they also acquire ellipsoidal and more elongated rod-like morphologies;[28,63,67,68] some of these elongated precipitates after 16- and 256-hour aging are marked by arrows in Figure 9(d, e, and g). The elongated morphology of Cu precipitates is attributed to a large anisotropy in the $\alpha$-Fe/Cu precipitate interfacial energy[68] and/or the shear associated with partial dislocations resulting in transformation to the 3R structure.[67] In the 64-hour aged sample, Figure 9(f), the observed platelet/disk-like morphology of the Cu precipitate is attributed to the additional consideration of elastic strain energy.[69]

$M_2C$ carbides are first observed in the 0.25-hour aged sample, Figure 9(b). In the 3D APT reconstructions of
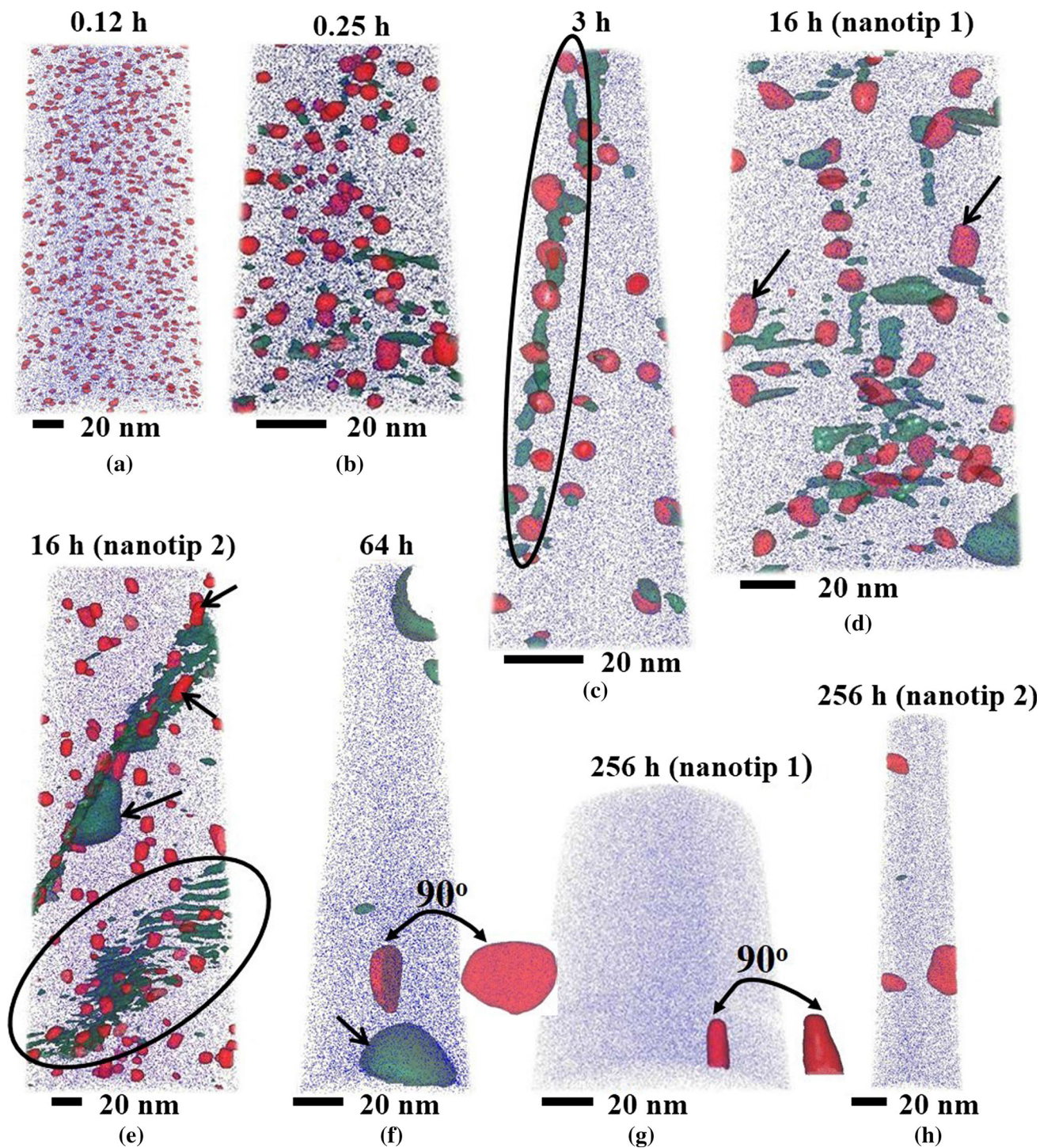
#### Table IV. Diffusion Coefficients of Different Elements in α-Fe at 823 K (550 °C)

| Element | Diffusion Coefficient (cm$^2$ s$^{-1}$) | References |
|---|---|---|
| C | $1.26 \times 10^{-7}$ | 45 |
| Mo | $1.54 \times 10^{-16}$ | 46 |
| Mn | $2.26 \times 10^{-15}$ | 47 |
| Cr | $1.06 \times 10^{-15}$ | 48 |
| Si | $7.93 \times 10^{-15}$ | 49 |

#### Table V. Chemical Composition (At. Pct) of the Core of the Cementite Precipitate Observed in HSLA-115 Aged at 823 K (550 °C) for 0.25 h and the Partitioning Ratios of Elements, as Obtained from APT Measurements

| Element | Fe | C | Mn | Cr | Cu | Ni | Mo | Si |
|---|---|---|---|---|---|---|---|---|
| APT-Measured Composition | $72.18 \pm 0.22$ | $22.71 \pm 0.21$ | $0.86 \pm 0.05$ | $0.71 \pm 0.04$ | $0.37 \pm 0.03$ | $2.24 \pm 0.08$ | $0.40 \pm 0.03$ | $0.16 \pm 0.02$ |
| Partitioning Ratio (APT) | $0.77 \pm 0.002$ | $34.56 \pm 1.74$ | $1.78 \pm 0.14$ | $1.63 \pm 0.14$ | $0.73 \pm 0.07$ | $0.78 \pm 0.03$ | $1.87 \pm 0.22$ | $0.31 \pm 0.04$ |
| Computed Composition, ThermoCalc | 40.59 | 25.0 | 9.08 | 23.89 | — | 0.31 | 0.76 | — |

Metastable equilibrium composition of cementite from thermodynamic computations at 823 K (550 °C) is also displayed.

Fig. 9—3D APT reconstructions of HSLA-115 samples aged at 823 K (550 °C) for (*a*) 0.12 h, (*b*) 0.25 h, (*c*) 3 h, (*d*) 16 h (nanotip 1), (*e*) 16 h (nanotip 2), (*f*) 64 h, (*g*) 256 h (nanotip 1), and (*h*) 256 h (nanotip 2). Only a fraction of the Fe atoms are shown (blue dots) and the other alloying element atoms are omitted for the sake of clarity. Copper precipitates are delineated by 10 at. pct Cu isoconcentration surfaces (red). $M_2C$ carbides are delineated by 5 at. pct (C + Cr + Mo) isoconcentration surfaces (dark green) in all reconstructions except in (*e*), where 7 at. pct (C + Cr + Mo) isoconcentration surfaces are used to delineate $M_2C$ carbides (Color figure online).

the 3- and 16-hour aged samples, elongated rod-like carbides are observed to be distributed heterogeneously along a dislocation line and at a martensitic lath boundary; see encircled regions in Figure 9(c) and Figure 9(e), respectively. $M_2C$ carbides are known to assume an elongated needle/rod-like morphology in $\alpha$-Fe[14,62,70–76] and grow along $\langle 100 \rangle_{\alpha\text{-Fe}}$ directions due to good lattice match along this direction.[70,76] As the carbide precipitates coarsen further, they assume irregular spheroidal morphologies, which is indicative of a

**Table VI.  Temporal Evolution of Mean Radius, $\langle R(t) \rangle$, Number Density, $N_v(t)$, and Volume Fraction, $\Phi$ (Pct), of Cu Precipitates in HSLA-115 Aged at 823 K (550 °C), data from Jain et al.[9]**

| Aging Time (h) | $\langle R(t) \rangle$ (nm) | $N_v(t)$ $(m^{-3})$ | $\Phi$ (Pct) |
| --- | --- | --- | --- |
| 0.12 | 1.34 ± 0.54 | $(7.22 \pm 0.14) \times 10^{23}$ | 0.61 ± 0.01 |
| 0.25 | 1.60 ± 0.81 | $(2.99 \pm 0.24) \times 10^{23}$ | 0.93 ± 0.07 |
| 1 | 3.36 ± 1.20 | $(7.30 \pm 0.55) \times 10^{22}$ | 1.61 ± 0.12 |
| 3 | 3.15 ± 0.95 | $(1.62 \pm 0.13) \times 10^{23}$ | 2.68 ± 0.22 |
| 16 | 5.09 ± 1.91 | $(3.24 \pm 0.19) \times 10^{22}$ | 2.53 ± 0.15 |

**Table VII.  Temporal Evolution of Mean Radius, $\langle R(t) \rangle$, Number Density, $N_v(t)$, and Volume Fraction, $\Phi$ (Pct), of $M_2C$ Carbide Precipitates in HSLA-115 Aged at 823 K (550 °C), data from Jain et al.[9]**

| Aging Time (h) | $\langle R(t) \rangle$ (nm) | $N_v(t)$ $(m^{-3})$ | $\Phi$ (Pct) |
| --- | --- | --- | --- |
| 0.25 | 1.07 ± 0.30 | $(7.10 \pm 1.17) \times 10^{22}$ | 0.05 ± 0.01 |
| 1 | 1.22 ± 0.42 | $(2.25 \pm 0.31) \times 10^{22}$ | 0.02 ± 0.003 |
| 3 | 1.64 ± 0.63 | $(1.46 \pm 0.13) \times 10^{23}$ | 0.40 ± 0.03 |
| 16 | 2.06 ± 1.62 | $(3.72 \pm 0.20) \times 10^{22}$ | 0.45 ± 0.02 |

loss of coherency with the matrix; two such carbides are indicated by arrows in Figure 9(e and f). The temporal evolution of the morphology of $M_2C$ carbides, as described above, is consistent with the findings of Liddle et al.,[73] who reported the transition of $M_2C$ carbides (in AF1410 steel) from small clusters to rods to larger irregular spheroidal particles with increasing aging times at 783 K (510 °C). We next describe the compositional evolution of Cu precipitates and $M_2C$ carbides at 823 K (550 °C).

Copper precipitates observed in the 0.12-hour aged sample (shortest aging time studied) contain ~50.0 at. pct Fe, which is consistent with the composition of Cu (b.c.c.) precipitates reported at early aging times in several other atom probe studies.[28,77–79] In contrast, negligible Fe concentrations have been reported in Cu precipitates from small-angle neutron scattering (SANS) studies.[80,81] While the composition of Cu precipitates at early aging times, as determined by APT, may be affected by the artificial inclusion of matrix Fe atoms due to ion trajectory overlaps,[82] the SANS-based analysis assumes the Cu precipitates in $\alpha$-Fe to be non-ferromagnetic, which is highly questionable in light of the significant Fe concentrations reported from atom probe studies. This remains an unresolved issue and has been discussed in detail elsewhere.[83] Cu precipitates observed at longer aging times have much higher Cu concentrations, which is consistent with other atom probe studies.[21,28,84] The average core composition of Cu precipitates in the 256-hour aged condition, Figure 9(h), is 91.4Cu-3.3Ni-4.2Mn-1.0Fe (at. pct). For all aging times studied, we observe the segregation of Ni and Mn at the $\alpha$-Fe/Cu precipitate interface, which has been reported and is attributed to the reduction in the interfacial energy of the heterophase interface.[28,78] We note that the Cu concentration measured in the $\alpha$-Fe matrix (excluding the Cu precipitates) after 256-hour aging is ~0.20 at. pct (0.23 wt pct), which is in excellent agreement with the experimentally determined Cu solubility of 0.21 wt pct in $\alpha$-Fe at 823 K (550 °C).[85] We

now discuss in detail the compositional evolution of $M_2C$ carbides by APT.

Proximity histogram concentration profiles of C, Mo, and Cr obtained for the respective ten largest $M_2C$ carbide precipitates in the 0.25-, 1-, 3-, and 16-hour (nanotip 1) aged samples are displayed in Figure 10, which reveal the enrichment of these elements in the carbide precipitates. The coarser blocky carbide precipitate observed to the bottom right in Figure 9(d) has been excluded from this analysis to obtain a well-defined analysis of the smaller carbide precipitates and to distinguish precipitates at different stages of their growth.

It is important to mention that in the 3D APT reconstruction, $M_2C$ carbide precipitates suffer from local magnification artifacts owing to their higher field evaporation strength than the matrix Fe atoms.[82] This leads to ion trajectory overlaps and results in artificial inclusion of matrix atoms in $M_2C$ carbides, which can complicate the evaluation of their compositions, particularly during early aging times. Additionally, carbon concentrations measured by APT can be influenced by the experimental variables, that is, specimen temperature[61] and laser pulse energy,[86] as has also been shown specifically for $M_2C$ carbides.[87,88] Working within these limitations, we focus on the temporal evolution of the atomic ratios (Mo + Cr)/C and Mo/Cr in the $M_2C$ carbide precipitates at 823 K (550 °C), rather than their absolute compositions.

However, compositions of coarser $M_2C$ carbide precipitates such as those indicated by arrows in Figure 9(e and f) can be determined with much greater accuracy and are described first. Their compositions, as determined using proximity histograms (displayed in Figure 11), are listed in Table VIII along with the computed composition of $M_2C$ carbide at thermodynamic equilibrium at 823 K (550 °C). The measured carbon concentrations of these two carbides are similar (30 to 31 at. pct) and in close agreement with the expected stoichiometric carbon concentration of 33.3 at.
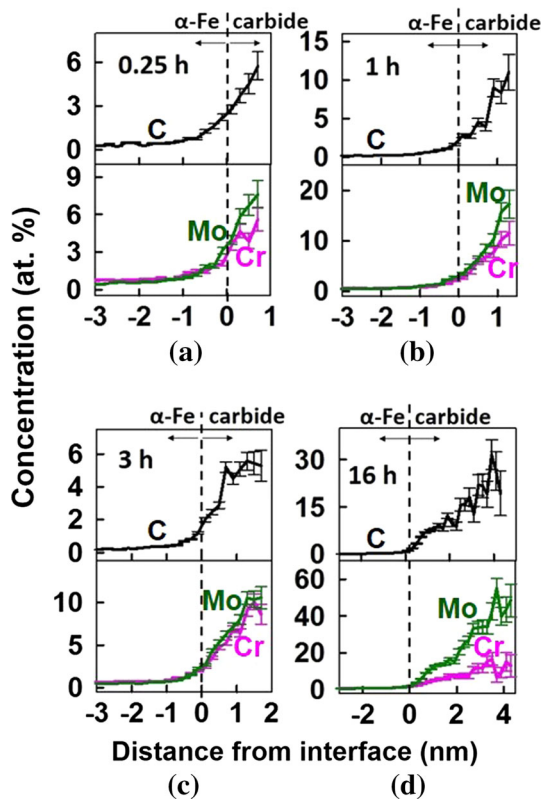
Fig. 10—Proximity histogram concentration profiles (at. pct) of C, Mo, and Cr for the ten largest $M_2C$ carbide precipitates and their vicinity in HSLA-115 samples aged at 823 K (550 °C) for (a) 0.25, (b) 1, (c) 3, and (d) 16 h (nanotip 1).



Fig. 11—Proximity histogram concentration profiles (at. pct) of Fe, Mo, C, and Cr for (a) $M_2C$ carbide [indicated by an arrow in Fig. 9(e)] and its vicinity; (b) $M_2C$ carbide [indicated by an arrow in Fig. 9(f)] and its vicinity. Figures 9(e) and (f) show the 3D APT reconstructions of HSLA-115 samples aged at 823 K (550 °C) for 16 and 64 h, respectively. A fiducial marker is placed vertically at the origin (0) of the proximity histograms, which is chosen as the inflection point of the Fe concentration profile.

pct in $M_2C$ carbides. Mass spectrum of the $M_2C$ carbide precipitate, which is indicated by an arrow in Figure 9(f), is displayed in Figure 12. Carbon mass peaks are obtained corresponding to $C^{2+}$, $C^+$, $C_3^{2+}$, $C_2^+$, and $C_3^+$ ions, Mo is observed in charge states $2+$ and $3+$, while Cr field evaporates primarily in charge state $2+$. It is noted that C and Mo are also obtained as combined molecular species in the form of $(MoC)^{2+}$. We now describe the temporal evolution of the atomic ratios $(Mo + Cr)/C$ and $Mo/Cr$ in the $M_2C$ carbide precipitates at 823 K (550 °C).

Figure 13 displays plots of the atomic ratios $(Mo + Cr)/C$ and $Mo/Cr$ for the ten largest $M_2C$ carbide precipitates and their vicinity in the 0.25-, 1-, 3-, and 16-hour (nanotip 1) aged samples; proximity histogram concentration profiles in Figure 10 were also obtained from these carbides. Since the matrix is mainly Fe, any contribution of Mo, Cr, and C from ion trajectory effects is not anticipated to affect the ratios of $(Mo + Cr)/C$ and $Mo/Cr$ significantly. Thus, these plots are helpful for discriminating the carbide precipitates from the matrix and in calibrating the potential compositional influence from ion trajectory effects. In Figure 13, we observe a gradual decrease in the $(Mo + Cr)/C$ atomic ratio from its value in the α-Fe matrix (left-hand side of the plots) toward the carbide precipitates (far right-hand side of the plots), where it approaches a plateau. This plateau region to the right-hand side of the vertical fiducial marker in Figure 13 is identified as the core of
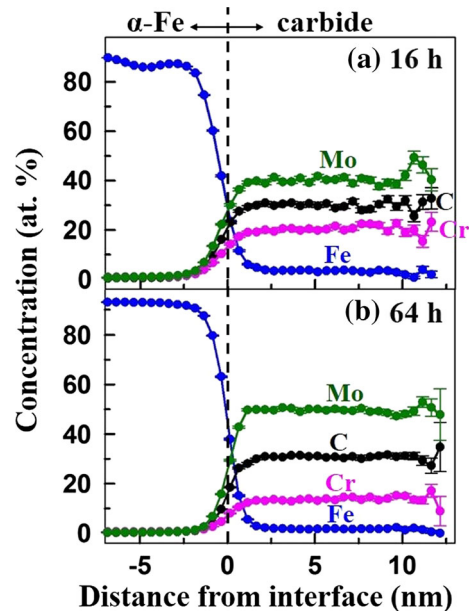
the $M_2C$ carbide precipitates, and the mean values of atomic ratios $(Mo + Cr)/C$ and $Mo/Cr$ obtained from these plateau regions for different aging times are displayed in Figure 14.

At early aging times of 0.25, 1, and 3 hours, $M_2C$ carbide precipitates are significantly sub-stoichiometric in carbon and have the $(Mo + Cr)/C$ atomic ratios of 2.5, 2.8, and 3.0, respectively, Figure 14(a). This ratio decreases to 2.2 for carbides in the 16-hour aged sample, thereby approaching the ideal value for $M_2C$ carbide stoichiometry. Sub-stoichiometric carbon concentrations in the $M_2C$ carbide precipitates have been previously reported.[25,62,73,75,89,90] Olson et al.[25] performed thermodynamic calculations to understand the compositional trajectory of $M_2C$ carbides in AF1410 steels, aged isothermally at 783 K (510 °C), and attributed lower carbon in the carbides at shorter aging times to the reduction in the interfacial energy of precipitating nuclei. For the coarser carbides, the proximity histogram analyses of which are displayed in Figure 11, the $(Mo + Cr)/C$ atomic ratio decreases to 2.0. It is noted that while the metal content of these $M_2C$ carbide precipitates consists primarily of Mo and Cr, they also contain some Mn, Fe, and very little V, Ni, and Cu, Table VIII. However, since their carbon concentrations measured by APT (30 to 31 at. pct) are less than the ideal 33.3 at. pct, the $(Mo + Cr)/C$ ratio of 2.0 in these carbides is slightly higher than the value of 1.9 obtained by equilibrium thermodynamic calculations, which also predict some Mn, V, and Fe in the $M_2C$ carbide, Table VIII.

**Table VIII. Compositions (at. pct) of M₂C Carbide Precipitates, Which are Indicated by Arrows in Fig. 9(e) and (f) in HSLA-115 Samples Aged at 823 K (550 °C) for 16 and 64 h, Respectively, as Obtained from APT Measurements and Equilibrium Composition of M₂C Carbide from Thermodynamic Computations at 823 K (550 °C)**

| Element | Mo | Cr | C | Fe | Mn | V | Ni | Cu |
|---|---|---|---|---|---|---|---|---|
| APT-Measured Composition, 16 h | 40.35 ± 0.43 | 20.49 ± 0.36 | 30.12 ± 0.40 | 3.43 ± 0.16 | 3.63 ± 0.16 | 0.20 ± 0.06 | 0.48 ± 0.06 | 0.30 ± 0.05 |
| APT-Measured Composition, 64 h | 49.76 ± 0.28 | 13.63 ± 0.19 | 30.91 ± 0.26 | 1.81 ± 0.07 | 2.62 ± 0.09 | 0.29 ± 0.03 | 0.26 ± 0.03 | 0.10 ± 0.02 |
| Computed Composition, ThermoCalc | 58.3 | 5.6 | 33.3 | 0.5 | 1.1 | 1.1 | — | 0.1 |
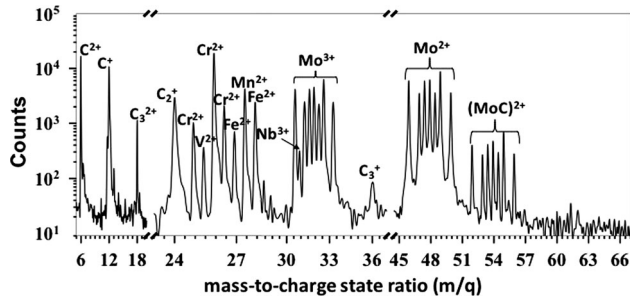


Fig. 12—Atom probe tomographic mass spectrum of the M₂C carbide precipitate observed in the HSLA-115 sample aged at 823 K (550 °C) for 64 h, which is indicated by an arrow in Fig. 9(f). It is noted that the abscissa scale chosen is not linear to enlarge portions of the mass spectrum for clarity.

The Mo/Cr atomic ratio in the M₂C carbide precipitates at early aging times of 0.25, 1, and 3 hours is nearly constant at ~1.3, but increases to 2.4 for carbides in the 16-hour aged sample, Figure 14(b). Substitution of Mo by Cr in M₂C carbide reduces its lattice parameter and is associated with the decrease in transformation strains.[76,91,92] Heterogeneous nucleation of M₂C carbides at Cu precipitates coupled with their sub-stoichiometric carbon composition, observed herein, further reduces the nucleation barrier for M₂C carbide precipitation. The Mo/Cr ratio increases further to 3.7 in the M₂C carbide precipitate analyzed in the 64-hour aged sample, while this ratio is 7.8 for the computed composition of M₂C at thermodynamic equilibrium, Table VIII. Thus, at early aging times, when M₂C carbide precipitates are presumably coherent, they have a smaller Mo/Cr ratio and sub-stoichiometric carbon concentrations. At longer aging times, the Mo/Cr ratio and the overall composition tends to approach the predicted composition at thermodynamic equilibrium.

## IV. SUMMARY AND CONCLUSIONS

For the first time, detailed compositional analysis of carbon redistribution and associated complex phase transformations are provided for an HSLA-115 steel, isothermally aged at 823 K (550 °C), which includes carbon segregation at lath boundaries, niobium carbonitride precipitates, cementite, M₂C carbide precipitates, and the synergetic interactions with Cu
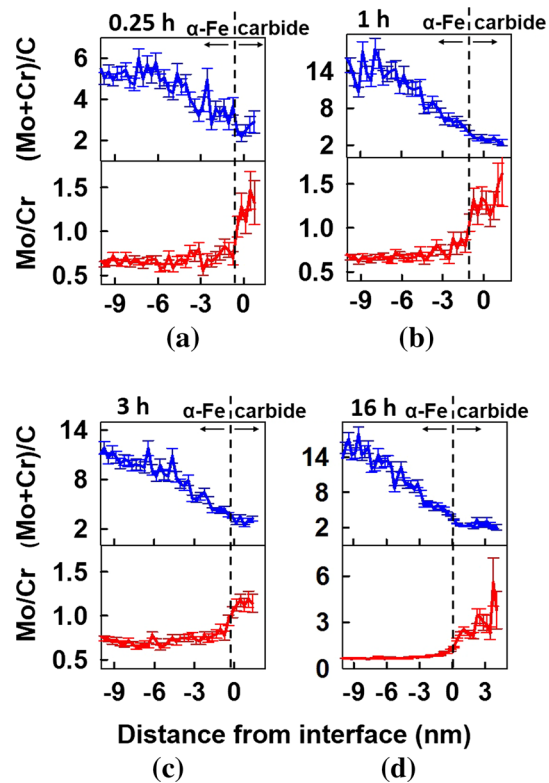


Fig. 13—Atomic ratios (Mo + Cr)/C and Mo/Cr for the ten largest M₂C carbides and their vicinity in HSLA-115 samples aged at 823 K (550 °C) for (a) 0.25 h, (b) 1 h, (c) 3 h, and (d) 16 h (nanotip 1). The portions of the diagrams on the right-hand side of the vertical fiducial markers in these plots represent the core of the M₂C carbide precipitates with nearly constant (Mo + Cr)/C values.

precipitation that happens simultaneously. The results are summarized in the conclusions below:

1. Segregation of carbon (3 to 6 at. pct C) is observed by 3D APT at martensitic lath boundaries in the as-quenched, Figure 3, and 0.12-hour aged samples, Figure 5(a), indicating that the diffusion of carbon occurs from the freshly formed martensite during quenching, following the austenitizing treatment. While Mn, Cr, and Mo are homogeneously distributed between the α-Fe matrix and the C-enriched regions in the as-quenched sample, Figure 4, their enrichment is observed in the C-enriched region in the 0.12-hour aged sample, Figure 5(b).
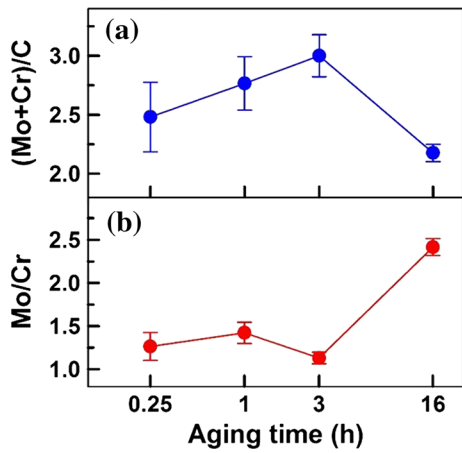
Fig. 14—Temporal evolution of atomic ratios: (*a*) (Mo + Cr)/C and (*b*) Mo/Cr in the $M_2C$ carbide precipitates for HSLA-115 aged at 823 K (550 °C). For aging times of 1, 3, and 16 h, these values are the mean values obtained from the analysis of the two APT nanotips for each of these aging times. Coarser blocky carbide precipitates observed to the bottom right in Fig. 9(d) and the one indicated by an arrow in Fig. 9(e) have been excluded from this analysis to obtain a clearer analysis of the smaller carbide precipitates and to distinguish precipitates at different stages of their growth.

On further aging, carbon is redistributed, forming cementite and $M_2C$ carbide precipitates.

2. Some carbon in the as-quenched microstructure is also associated with niobium carbonitride precipitates, as they do not dissolve during the austenitizing treatment. Composition of one such precipitate observed in the 3D APT reconstruction of the as-quenched sample, Figure 3, having a thin platelet-like morphology, is 43.2Nb-41.6C-9.8N-2.7Mo-1.1Cr-0.5V-0.5Fe (at. pct) or 79.9Nb-10.0C-2.7N-5.2Mo-1.1Cr-0.5V-0.6Fe (wt pct). These precipitates are also present in the microstructure after aging at 823 K (550 °C) for 0.25, 3, and 16 hours, as confirmed by synchrotron XRD, Figure 2(a).

3. Cementite formation occurs during aging at 823 K (550 °C), Figure 2(a). Carbon-enriched regions at lath boundaries, Figures 3 and 5(a), and the decomposition of retained austenite and lath martensite in the as-quenched microstructure are the likely sources of carbon for cementite formation. Core composition of the cementite precipitate observed in the 3D APT reconstruction of the 0.25-hour aged sample, Figure 7, is 72.0Fe-22.7C-2.5Ni-0.9Mn-0.7Cr-0.4-Mo-0.4Cu-0.2Si (at. pct) or 87.5Fe-5.9C-3.2-Ni-1.1Mn-0.8Cr-0.8Mo-0.6Cu-0.1Si (wt pct). Mn, Cr, and Mo partition to the cementite precipitate, while Si is rejected from it. A much higher degree of enrichment of Mn, Cr, and Mo is observed near the cementite/α-Fe interface than in the core of the cementite precipitate, which is attributed to their sluggish diffusion kinetics.

4. The precipitation kinetics of $M_2C$ carbides and Cu precipitates are closely intertwined at 823 K (550 °C). Their precipitation sequence coupled with co-located nature suggests that Cu precipitates catalyze the nucleation of $M_2C$ carbides,

Figure 9(a, b, and c). $M_2C$ carbides assume elongated rod-like morphologies as they grow and coarsen; a significant fraction of these are observed to be distributed heterogeneously along a dislocation line and at a martensitic lath boundary, Figure 9(c and e), respectively. On further aging and consequent coarsening, they acquire irregular spheroidal morphology, Figure 9(f).

5. The compositional evolution of $M_2C$ carbide precipitates during aging at 823 K (550 °C) is described by measuring the atomic ratios (Mo + Cr)/C and Mo/Cr in the core of the carbide precipitates using 3D APT. At early aging times of 0.25, 1, and 3 hours, $M_2C$ carbides are significantly sub-stoichiometric in carbon with the (Mo + Cr)/C atomic ratio varying from 2.5 to 3, and they have a nearly constant Mo/Cr atomic ratio of ~1.3, Figure 14. On further aging, their composition tends to approach the computed composition at thermodynamic equilibrium at 823 K (550 °C), with a nearly stoichiometric carbon concentration and a higher Mo/Cr atomic ratio. Composition of one such $M_2C$ carbide precipitate observed in the 64-hour aged sample is 49.8Mo-13.3Cr-30.9C-2.1Fe-2.6Mn-0.3V-0.3Ni-0.1 Cu (at. pct) or 77.8Mo-11.3Cr-6.0C-1.9Fe-2.3Mn-0.2V-0.3Ni-0.1Cu (wt pct).

## REFERENCES

1. A.D. Wilson, E.G. Hamburg, D.J. Colvin, S.W. Thompson, and G. Krauss: *Microalloyed HSLA Steels*, Metals Park, OH, ASM International, 1988, pp. 259–75.
2. E.J. Czyryca, R.E. Link, R.J. Wong, D.A. Aylor, T.W. Montemarano, and J.P. Gudas: *Nav. Eng. J.*, 1990, vol. 102, pp. 63–82.
3. L.G. Kvidahl: *Weld. J.*, 1985, vol. 64, pp. 42–48.

4. C.S. Smith and E.W. Palmer: *Trans. AIME*, 1933, vol. 104, pp. 133–68.
5. E.J. Czyryca: *Key Eng. Mater.*, 1993, vol. 84, pp. 491–520.
6. P.J. Konkol, K.M. Stefanick, and G.S. Pike: *Weld. J.*, 2011, vol. 90, pp. 34–41.
7. C. Revising: Report No. GAO-15-22, United States Government Accountability Office, Washington, DC, November 2014.
8. R.P. Foley and M.E. Fine: *International Conference on Processing, Microstructure and Properties of Microalloyed and Other Modern High Strength Low Alloy Steels*, Warrendale, PA, 1991, pp. 315–30.
9. D. Jain, D. Isheim, A.H. Hunter, and D.N. Seidman: *Metall. Mater. Trans. A*, 2016, vol. 47A, pp. 3860–72.
10. G. Spanos, R.W. Fonda, R.A. Vandermeer, and A. Matuszeski: *Metall. Mater. Trans. A*, 1995, vol. 26A, pp. 3277–93.
11. L.J. Cuddy and J.C. Raley: *Metall. Trans. A*, 1983, vol. 14A, pp. 1989–95.
12. T. Gladman: *Proc. R. Soc. A*, 1966, vol. 294, pp. 298–309.
13. M. Shome, D.S. Sarma, O.P. Gupta, and O.N. Mohanty: *ISIJ Int.*, 2003, vol. 43, pp. 1431–37.
14. G.R. Speich, D.S. Dabkowski, and L.F. Porter: *Metall. Trans.*, 1973, vol. 4, pp. 303–15.
15. G. Krauss: *Steels: Processing, Structure, and Performance*, Materials Park, OH, ASM International, 2005, pp. 338–39.
16. B. Gault, M.P. Moody, J.M. Cairney, and S.P. Ringer: *Atom Probe Microscopy*, Springer, New York, NY, 2012.
17. T.F. Kelly and M.K. Miller: *Rev. Sci. Instrum.*, 2007, vol. 78, p. 031101.
18. D.N. Seidman: *Annu. Rev. Mater. Res.*, 2007, vol. 37, pp. 127–58.
19. A. Saha and G.B. Olson: *J. Comput. Aided Mater. Des.*, 2007, vol. 14, pp. 177–200.
20. A. Saha, J. Jung, and G.B. Olson: *J. Comput. Aided Mater. Des.*, 2007, vol. 14, pp. 201–33.
21. M.D. Mulholland and D.N. Seidman: *Acta Mater.*, 2011, vol. 59, pp. 1881–97.
22. J.S. Wang, M.D. Mulholland, G.B. Olson, and D.N. Seidman: *Acta Mater.*, 2013, vol. 61, pp. 4939–52.
23. D. Raabe, S. Sandlöbes, J. Millán, D. Ponge, H. Assadi, M. Herbig, and P.P. Choi: *Acta Mater.*, 2013, vol. 61, pp. 6132–52.
24. R.C. Thomson and M.K. Miller: *Acta Mater.*, 1998, vol. 46, pp. 2203–13.
25. G.B. Olson, T.J. Kinkus, and J.S. Montgomery: *Surf. Sci.*, 1991, vol. 246, pp. 238–45.
26. A. Afrouz, M.J. Collins, and R. Pilkington: *Metals Technology*, 1983, vol. 10, pp. 461–63.
27. O.C. Hellman, J.A. Vandenbroucke, J. Rüsing, D. Isheim, and D.N. Seidman: *Microsc. Microanal.*, 2000, vol. 6, pp. 437–44.
28. R.P. Kolli and D.N. Seidman: *Acta Mater.*, 2008, vol. 56, pp. 2073–88.
29. B.D. Cullity and S.R. Stock: *Elements of X-ray Diffraction*, 3rd ed., Prentice Hall, Upper Saddle River, NJ, 2001, p. 351.
30. S.K. Dhua, D. Mukerjee, and D.S. Sarma: *Metall. Mater. Trans. A*, 2001, vol. 32A, pp. 2259–70.
31. F.D. Geuser and W. Lefebvre: *Microsc. Res. Tech.*, 2011, vol. 74, pp. 257–63.
32. S. Morito, K. Oh-ishi, K. Hono, and T. Ohba: *ISIJ Int.*, 2011, vol. 51, pp. 1200–02.
33. L. Morsdorf, C.C. Tasan, D. Ponge, and D. Raabe: *Acta Mater.*, 2015, vol. 95, pp. 366–77.
34. M.K. Miller, P.A. Beaven, and G.D.W. Smith: *Metall. Trans. A*, 1981, vol. 12, pp. 1197–1204.
35. C. Lerchbacher, S. Zinner, and H. Leitner: *Micron*, 2012, vol. 43, pp. 818–26.
36. B. Hutchinson, J. Hagström, O. Karlsson, D. Lindell, M. Tornberg, F. Lindberg, and M. Thuvander: *Acta Mater.*, 2011, vol. 59, pp. 5845–58.
37. G. Krauss: *Mater. Sci. Eng. A*, 1999, vol. 273, pp. 40–57.
38. K.W. Andrews: *J. Iron Steel Inst.*, 1965, vol. 203, pp. 721–27.
39. G.R. Speich: *Trans. Met. Soc. AIME*, 1969, vol. 245, pp. 2553–64.
40. E. Bemont, E. Cadel, P. Maugis, and D. Blavette: *Surf. Interface Anal.*, 2004, vol. 36, pp. 585–88.
41. R.P. Kolli and D.N. Seidman: *Microsc. Microanal.*, 2014, vol. 20, pp. 1727–39.
42. A.J. Breen, K.Y. Xie, M.P. Moody, B. Gault, H.W. Yen, C.C. Wong, J.M. Cairney, and S.P. Ringer: *Microsc. Microanal.*, 2014, vol. 20, pp. 1100–10.
43. K. Miyata, T. Kushida, T. Omura, and Y. Komizo: *Metall. Mater. Trans. A*, 2003, vol. 34A, pp. 1565–73.
44. W. Sha, L. Chang, G.D.W. Smith, L. Cheng, and E.J. Mittemeijer: *Surf. Sci.*, 1992, vol. 266, pp. 416–23.
45. J.K. Stanley: *Trans. AIME*, 1949, vol. 185, pp. 752–61.
46. V.T. Borisov, V.M. Golikov, and G.V. Sherbedinskiy: *Phys. Met. Metallogr*, 1966, vol. 22, pp. 175–76.
47. C.J. Smithells, E.A. Brandes, and G.B. Brook: *Smithells Metals Reference Book*, Butterworth-Heinemann, Oxford, 1992.
48. A.W. Bowen and G.M. Leak: *Metall. Trans.*, 1970, vol. 1, pp. 1695–1700.
49. R.J. Borg and D.Y.F. Lai: *J. Appl. Phys.*, 1970, vol. 41, pp. 5193–5200.
50. G. Ghosh and G.B. Olson: *Acta Mater.*, 2002, vol. 50, pp. 2099–2119.
51. W. Song, J. von Appen, P. Choi, R. Dronskowski, D. Raabe, and W. Bleck: *Acta Mater.*, 2013, vol. 61, pp. 7582–90.
52. S.S. Babu, K. Hono, and T. Sakurai: *Metall. Mater. Trans. A*, 1994, vol. 25A, pp. 499–508.
53. L. Chang and G.D.W. Smith: *Le Journal de Physique Colloques*, 1984, vol. 45, pp. C9-397–C9-401.
54. C. Zhu, X.Y. Xiong, A. Cerezo, R. Hardwicke, G. Krauss, and G.D.W. Smith: *Ultramicroscopy*, 2007, vol. 107, pp. 808–12.
55. M. Thuvander, J. Weidow, J. Angseryd, L.K.L. Falk, F. Liu, M. Sonestedt, K. Stiller, and H.O. Andrén: *Ultramicroscopy*, 2011, vol. 111, pp. 604–08.
56. D.W. Saxey: *Ultramicroscopy*, 2011, vol. 111, pp. 473–79.
57. R.P. Kolli and D.N. Seidman: *Microsc. Microanal.*, 2007, vol. 13, pp. 272–84.
58. W.S. Owen: *Trans. ASM*, 1954, vol. 46, pp. 812–29.
59. H.K.D.H. Bhadeshia and D.V. Edmonds: *Metall. Trans. A*, 1979, vol. 10A, pp. 895–907.
60. G. Miyamoto, J.C. Oh, K. Hono, T. Furuhara, and T. Maki: *Acta Mater.*, 2007, vol. 55, pp. 5027–38.
61. J. Takahashi, K. Kawakami, and Y. Kobayashi: *Ultramicroscopy*, 2011, vol. 111, pp. 1233–38.
62. B.L. Tiemens, A.K. Sachdev, R.K. Mishra, and G.B. Olson: *Metall. Mater. Trans. A*, 2012, vol. 43A, pp. 3626–35.
63. R.C. Glenn and E. Hornbogen: *Trans. Metall. Soc. AIME*, 1960, vol. 218, pp. 1064–70.
64. S.R. Goodman, S.S. Brenner, and J.R. Low: *Metall. Trans.*, 1973, vol. 4, pp. 2363–69.
65. S. Pizzini, K.J. Roberts, W.J. Phythian, C.A. English, and G.N. Greaves: *Philos. Magn. Lett.*, 1990, vol. 61, pp. 223–29.
66. P.J. Othen, M.L. Jenkins, G.D.W. Smith, and W.J. Phythian: *Philos. Magn. Lett.*, 1991, vol. 64, pp. 383–91.
67. P.J. Othen, M.L. Jenkins, and G.D.W. Smith: *Philos. Magn. A*, 1994, vol. 70, pp. 1–24.
68. G.R. Speich and R.A. Oriani: *Trans. Met. Soc. AIME*, 1965, vol. 233, pp. 623–31.
69. F.R.N. Nabarro: *Proc. R. Soc. A*, 1940, vol. 175, pp. 519–38.
70. D.J. Dyson, S.R. Keown, D. Raynor, and J.A. Whiteman: *Acta Metall.*, 1966, vol. 14, pp. 867–75.
71. D. Raynor, J.A. Whiteman, and R.W.K. Honeycombe: *Iron Steel Inst. J.*, 1966, vol. 204, pp. 349–54.
72. W. Rong and G.L. Dunlop: *Acta Metall.*, 1984, vol. 32, pp. 1591–99.
73. J.A. Liddle, G.D.W. Smith, and G.B. Olson: *Le Journal de Physique Colloques,* 1986, vol. 47, pp. C7-223–C7-31.
74. Y.N. Shi and P.M. Kelly: *J. Mater. Sci.*, 2002, vol. 37, pp. 2077–85.
75. J. Akré, F. Danoix, H. Leitner, and P. Auger: *Ultramicroscopy*, 2009, vol. 109, pp. 518–23.
76. J.S. Montgomery and G.B. Olson: Innovations in Ultrahigh Strength Steel Technology, in *Proceeding of 34th Sagamore Army Materials Research Conference*, G.B. Olson, M. Azrin, and E.S. Wright, eds., US Army Materials Technology Laboratory, Watertown, MA, 1990, pp 147–78.
77. S.R. Goodman, S.S. Brenner, and J.R. Low: *Metall. Trans.*, 1973, vol. 4, pp. 2371–78.
78. D. Isheim, M.S. Gagliano, M.E. Fine, and D.N. Seidman: *Acta Mater.*, 2006, vol. 54, pp. 841–49.
79. D. Isheim, R.P. Kolli, M.E. Fine, and D.N. Seidman: *Scr. Mater.*, 2006, vol. 55, pp. 35–40.

80. F. Maury, N. Lorenzelli, and C.H. De Novion: *J. Nucl. Mater.*, 1991, vol. 183, pp. 217–20.
81. K. Osamura, H. Okuda, K. Asano, M. Furusaka, K. Kishida, F. Kurosawa, and R. Uemori: *ISIJ Int.*, 1994, vol. 34, pp. 346–54.
82. F. Vurpillot, A. Bostel, and D. Blavette: *Appl. Phys. Lett.*, 2000, vol. 76, pp. 3127–29.
83. M.E. Fine, J.Z. Liu, and M.D. Asta: *Mater. Sci. Eng. A*, 2007, vol. 463, pp. 271–74.
84. M. Kapoor, D. Isheim, G. Ghosh, S. Vaynman, M.E. Fine, and Y.W. Chung: *Acta Mater.*, 2014, vol. 73, pp. 56–74.
85. M. Perez, F. Perrard, V. Massardier, X. Kleber, A. Deschamps, H. De Monestrol, P. Pareige, and G. Covarel: *Philos. Magn.*, 2005, vol. 85, pp. 2197–2210.
86. F. Liu and H.O. Andrén: *Ultramicroscopy*, 2011, vol. 111, pp. 633–41.
87. M.D. Mulholland and D.N. Seidman: *Microsc. Microanal.*, 2011, vol. 17, pp. 950–62.
88. G.M. Carinci, M.G. Hetherington, and G.B. Olson: *Le Journal de Physique Colloques,* 1988, vol. 49, pp. C6-311–C6-16.
89. H.F. Fischmeister, S. Karagöz, and H.O. Andren: *Acta Metall.*, 1988, vol. 36, pp. 817–25.
90. K. Stiller, L.E. Svensson, P.R. Howell, W. Rong, H.O. Andren, and G.L. Dunlop: *Acta Metall.*, 1984, vol. 32, pp. 1457–67.
91. H. Morikawa, H. Komatsu, and M. Tanino: *J. Electron Microsc.*, 1973, vol. 22, pp. 99–101.
92. R. Ayer and P.M. Machmeier: *Metall. Mater. Trans. A*, 1996, vol. 27A, pp. 2510–17.